JOURNAL OF MATERIALS SCIENCE **32** (1997) 6415–6427

Drying shrinkage of cement paste as measured in an environmental scanning electron microscope and comparison with microstructural models

C. M. NEUBAUER*, T. B. BERGSTROM*, K. SUJATA*, Y. XI§,
E. J. GARBOCZI‖, H. M. JENNINGS*
**Departments of Materials Science and Engineering and Civil Engineering, Northwestern University, Evanston, IL 60208, USA*
§Department of Civil Engineering, Drexel University, Philadelphia, PA 19104, USA
‖National Institute of Standards and Technology, Gaithersburg, MD 20899, USA

A recently developed image-intensity-matching technique has been used to analyse images of cement paste which were dried in an environmental scanning electron microscope. Shrinkage that occurs during changes in relative humidity is reported, together with some of the influences of water-to-cement ratio, temperature and age. Results from microstructurally based models are compared with experimental results. The best fit of models to experiment is achieved if calcium silicate hydrate (C–S–H) is divided into two types: high density C–S–H, which does not shrink, and low density C–S–H, which does shrink. Approximate values of unrestrained shrinkage of the low density C–S–H are attained as a function of relative humidity.

1. Introduction

The reaction of ordinary portland cement (OPC) and water produces cement paste, which composes the matrix phase in concrete. From the millimetre to meter length scale, concrete is a complex composite composed of cement paste, various additives and aggregates. However, on the micrometre length scale, cement paste itself is a complex composite. Two important products in cement paste are calcium silicate hydrate (C–S–H) and calcium hydroxide (CH)[1]. C–S–H is nearly amorphous and has a variable composition. The atomic structure of C–S–H is not well understood, but it is probably a layered material [1, 2] which is an assemblage of imperfect tobermorite [3] and possibly jennite [4], with a water content dependent on the relative humidity of the local environment [5]. Depending on the measurement technique used, the surface area of C–S–H ranges between 200 and 600 $m^2 g^{-1}$ of D-dried C–S–H (C–S–H equilibrated with ice at $-79\,^{\circ}C$) [1, 5]. In contrast with C–S–H, CH has a fixed composition and the atomic structure is known. Portland cement paste also contains various other phases such as ettringite, ferrites and aluminates.

An important property of hardened cement paste is drying shrinkage, the strain associated with loss of water. Drying shrinkage has been explained by mechanisms that include capillary tension, changes in surface energy, loss of interlayer water, and disjoining pressure [6]. Most of the drying shrinkage occurs in the C–S–H, while CH, anhydrous cement and aggregate all restrain shrinkage. Although the aluminate and ferrite phases may shrink somewhat, they are generally only present in relatively small quantities and are not considered in this paper.

One mechanism that causes shrinkage between 100 and 40% relative humidity is capillary stress, resulting from menisci that form in the capillary pores upon drying. As liquid evaporates, the tension in the menisci is transferred to the pore walls, causing contraction and resulting shrinkage [5, 7–11]. Also within this relative humidity range, disjoining pressure may be important [5, 7–9]. The mechanism of disjoining pressure is defined the following way. In a saturated state, a thick layer of water is adsorbed on the surfaces of adjoining C–S–H particles, creating a repulsive force. As the relative humidity is lowered, adsorbed water is removed, causing the water layer to become thinner, which results in shrinkage.

Gibbs–Bangham shrinkage operates at lower relative humidities (less than 40%) [5, 7–11]. Unsatisfied surface bonds on the C–S–H layers cause a high surface free energy, which in turn results in a high surface tension. Adsorbed water molecules will decrease this surface free energy. As the relative humidity is lowered, these adsorbed water molecules leave, causing increased attraction between C–S–H particles, and shrinkage. The maximum shrinkage occurs with the removal of the last adsorbed water layer.

---

[1] In cement chemistry notation, C = CaO, S = SiO_2 and H = H_2O.

0022–2461

A final mechanism, which operates at only the lowest relative humidities (less than 11%), is the loss of interlayer water [5, 7–11]. This is essentially the same as disjoining pressure except that it occurs between the layers of a single C–S–H particle, rather than between C–S–H particles. As the adsorbed water is removed, the C–S–H layers collapse, perhaps resulting in irreversible shrinkage [2].

A distinction between *real* and *apparent* mechanisms has been made [12]. Real mechanisms are associated with the material properties of cement paste and are independent of specimen geometry. Apparent mechanisms are dependent upon specimen geometry. For example, a moisture gradient across a thick specimen may occur upon drying and the subsequent differential shrinkage results in cracking, which alters the bulk shrinkage response. Thus, in order to determine real mechanisms, specimens that do not have stress gradients must be used. Measurements of real shrinkage can be made by using extremely thin samples and/or lowering humidity so slowly that the moisture gradient is minimized. Very thin samples are often difficult to handle or are too small for measurements to be attained. Lowering relative humidity slowly can require an experiment time that is simply too long.

Ideally, a real *unrestrained* shrinkage value for C–S–H, as a function of relative humidity, could be determined for use in recently developed computer-based microstructural models that can be used for predicting properties [13]. These models require unrestrained shrinkage and elastic properties of each phase as input. The unrestrained shrinkage value is the strain that a pure phase will develop at a given relative humidity. Values for most phases are available but those for C–S–H are unknown. Larger-scale experimental results can be compared with model results only if specific drying shrinkage strain values for C–S–H can be assigned. However, even for thin cement samples, measured shrinkage values are for a complex composite of shrinking and restraining phases. Unrestrained shrinkage of C–S–H can only be measured on samples which do not contain other phases such as CH, unreacted cement or porosity. Therefore, unrestrained shrinkage of C–S–H can only be measured on a tiny sample of material that is not connected to any restraint. In cement, this requires a region of C–S–H to be observed on the micrometre scale, which has only distant connections to a restraining phase.

The results reported here are an attempt to probe the unrestrained shrinkage of C–S–H. An environmental scanning electron microscope and a new image analysis technique were used to measure drying shrinkage of very small specimens of hardened cement paste *in situ*. Specimens were maintained in an atmosphere containing water vapour at relative humidities between 5 and 80% within the environmental scan-ning electron microscope [14, 15]. In conjunction with the microscope technique, an image-intensity-matching technique (IIMT) [16] has been developed to analyse deformation of the microstructure.

Results of *in situ* measurements of displacements during drying are reported and are discussed in terms of possible shrinkage mechanisms. Some of the values for shrinkage of the smallest particles may approach values for unrestrained shrinkage. Reasonable agreement is found between these values and those required as input to microstructurally based models for prediction of macrostrains. Initial results are given for shrinkage of very small samples and values that approach unrestrained shrinkage of C–S–H.

2. Experimental techniques

2.1. Sample preparation

Pastes were made from a type I OPC. After cement and deionized water were mixed by hand for 5 min at various water-to-cement mass ratios, *w/c*, pastes were cast in small cylinders, sealed, rotated for a minimum of 4 h to avoid sedimentation and then stored at 20 °C. After 24 h, the cylinders were demolded and cured in a lime-saturated water bath maintained at an appropriate temperature. The curing temperature, *w/c* and age of the samples were varied. The degree of hydration or percentage reacted was determined for each paste using the loss-on-ignition (LOI) technique.

2.2. Observations in the environmental scanning electron microscope

As soon as the sample was placed in the environmental scanning electron microscope, the chamber was pumped to a relative humidity of 80% and held for 10 min before the first image was taken. A fracture flake approximately 1 cm^2 in area and 1 mm thick was used and, as far as was possible, reasonably flat regions of the fracture surface were examined in each experiment. The relative humidity was varied by changing the chamber pressure, while the sample was maintained at a temperature of 10 °C.

Images were taken at magnifications of 1000 × and 5000 ×, which allowed observation of a small area containing a number of particles or a single hydrated particle, respectively. Images taken at 1000 × magnification were used to study *area* shrinkage, an area several hundred micrometres across which includes restraining phases. Images taken at 5000 × magnification were used to study *particle* shrinkage, the shrinkage of a single C–S–H particle, which should approach the unrestrained shrinkage for this phase. The field of view at 5000 × magnification was approximately 20 μm wide. The single particle was chosen to be a particle separated from the rest. Often this was a particle sitting above the general fracture plane. At each relative humidity, the sample was held for 10 min before imaging. A typical sequence included images obtained at 80%, 60%, 40%, 20% and 5% relative humidity. The final image at 5% relative humidity could not be obtained directly because the detector requires a minimum gas pressure greater than that present at 5% relative humidity in order to form an image. This image was taken by momentarily increasing the pressure to 20% relative humidity after 10 min at 5% relative humidity. All images were 512×512 pixels in size.

2.3. Image-intensity matching technique

Because the magnitude of shrinkage for cement paste is relatively small, typically less than 1%, deformation was not detectable by simple visual comparison of environmental scanning electron microscopy (ESEM) images. Even if transparencies were overlaid, no displacements could be observed, much less evaluated quantitatively. The IIMT takes two images as input and computes the magnitude of deformations at various locations in the image. The results reported here represent the first use of the IIMT.

The methodology for IIMT computation is as follows. Two images are required: a *reference* image, taken prior to deformation, and a *deformed* image, in which drying shrinkage has occurred. In this study, the reference image was taken at 80% relative humidity; any shrinkage taking place between 100% and 80% relative humidity was ignored. The deformed images were those taken at relative humidities lower than 80%. From the deformed image, a pixel of interest is chosen and a 20 pixel square window, called the *search window*, is centred at that pixel. A large *reference window*, 40 pixels square, is centred at the same location in the reference image. In order to remove as much variation in contrast as possible, the intensities of these two windows are modified to a distribution with mean of zero and standard deviation of 1. This technique removes most of the variation in contrast and brightness between images, then, the search window is systematically moved and distorted over the reference window. For each incremental distortion, one image is subtracted from the other until a minimum mean square error criterion is satisfied.

In simple terms, this technique finds the deformations of the search window which minimize the difference between the intensity surfaces of this window and the reference window. The deformation required to realign the deformed image to the reference image is equal and opposite to the deformation experienced during drying. The algorithm is capable of evaluating igid-body translation, expansion or contraction, and shear.

An important ramification of this technique is that subpixel deformations are determined. This occurs because the comparison of two windows is not based solely on discrete pixels but instead interpolates between pixels and is, in effect, a comparison between two intensity surfaces. Because surfaces are being mapped, no sharp edges are required. The only requirement is that the region of interest, or window, has a non-uniform pattern of grey levels [16]. One way of testing the resolution of IIMT is to artificially shift a computer-generated image and then to have the computer measure this shift. This test indicates that the IIMT has a practical resolution of approximately 0.2 pixels [16].

All shrinkage measurements reported here were calculated by comparing the length between two widely spaced points ($N \approx 200$ pixels apart) at a specific relative humidity (60% or less) to the reference length in the image taken at 80% relative humidity. Each shrinkage measurement is the average of six separate measurements involving many points on different parts of the sample. Typical scatter due to variation in samples was about 20% of the measured strain.

2.3.1. *Effect of scale on the image-intensity-matching technique*

The effect of scale on the resolution of the IIMT is an important consideration. A simple mathematical proof will show that magnification has no effect on the analyses in this paper provided that the specific points of interest are spaced adequately.

Consider two points of interest separated by a line which is N pixels long, where each pixel has length a, so that the initial length of this line is Na. However, there is some inherent error in the digitization of the image, since only the predominant grey level in each pixel is assigned. Therefore, as shown in Fig. 1, features (grey region) which slightly overlap adjoining pixels are considered the same as features which do not entirely fill their own pixels. This error is of the order of ± 0.5 pixels, so accounting for this on both ends of the line gives an initial measured length L_i of

$$L_\mathrm{i} = Na \pm a = a(N \pm 1) \tag{1}$$

Now displace the points of interest so that the line is strained by 10%, or $0.1Na$. Using the IIMT to determine those displacements introduces an error of ± 0.2 pixels ($\pm 0.2a$) at both ends of the line. Again, accounting for the initial digitization error and summing gives a final measured length of

$$L_\mathrm{f} = Na + 0.1Na \pm 0.4a \pm a = a(1.1N \pm 1.4) \tag{2}$$

Using the fundamental definition for engineering strain [17] given by

$$\varepsilon_\mathrm{E} = \frac{\delta l}{l_0} \tag{3}$$

and using Equations 1 and 2 in Equation 3 gives

$$\varepsilon_\mathrm{E} = \frac{L_\mathrm{f} - L_\mathrm{i}}{L_\mathrm{i}} = \frac{a(1.1N \pm 1.4) - a(N \pm 1)}{a(N \pm 1)} = \frac{0.1N \pm 2.4}{N \pm 1} \tag{4}$$

Thus, in considering widely separated points in which $N \approx 200$, which is applicable for the strains calculated in this paper, Equation 4 reduces to

$$\varepsilon_\mathrm{E} \approx 0.1 \tag{5}$$

with an error in the strain of approximately $2.4/N$ or 1%.

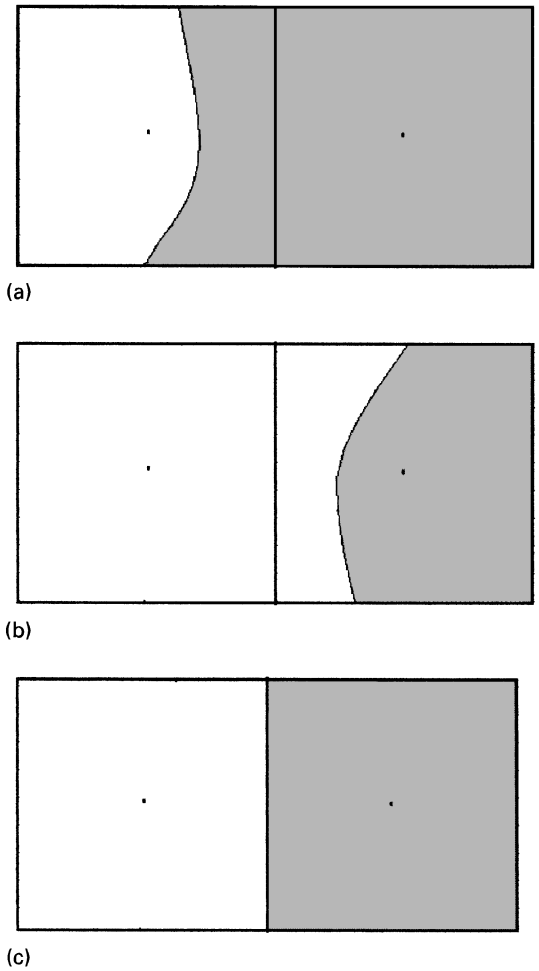

Figure 1 Illustration of digitization process: (a) feature of interest overlaps adjoining pixel; (b) feature of interest does not fill primary pixel; (c) digitized image for both (a) and (b).

Now increase the magnification by a factor of 20 so that the same line is now initially $20N$ pixels long, strain it by 10% and recalculate Equations 1, 2, 4 and 5:

$$L_i = 20Na \pm a = a(20N \pm 1) \tag{6}$$

$$\begin{aligned} L_f &= 20Na + 2Na \pm 0.4a \pm a \\ &= a(22N \pm 1.4) \end{aligned} \tag{7}$$

$$\begin{aligned} \varepsilon_E &= \frac{L_f - L_i}{L_i} = \frac{a(22N \pm 1.4) - a(20N \pm 1)}{a(20N \pm 1)} \\ &= \frac{2N \pm 2.4}{20N \pm 1} \end{aligned} \tag{8}$$

$$\varepsilon_E \approx 0.1 \tag{9}$$

with an error in the strain of approximately $2.4/20N$ or 0.06% when $N \approx 200$. As is evident from Equations 5 and 9, the analysis is both accurate and unaffected by magnification for widely spaced points.

2.3.2. Three-dimensional versus two-dimensional considerations

Another point of concern in the IIMT is the use of two-dimensional (2D) images to represent the three-dimensional (3D) mechanisms occurring during deformation. As stated previously, the samples used were flakes, approximately 1 mm thick, and about 1 cm^2 in area. These are definitely 3D samples and were approximately unrestrained in all three dimensions. The shape of the samples implies that, if we were to think of them as 2D samples, we should use the plane-stress hypothesis, which is more applicable to thin samples [18]. The IIMT simply measures the shrinkage strain in two dimensions only. For an isotropic sample, the shrinkage strains are the same in every direction, so that those measured in the plane are valid 3D strains. For macroscopic samples, such as a bar of cement paste, one typically measures length changes in only one dimension and makes the assumption of sample isotropy, just as the IIMT does.

Is cement homogeneous and isotropic on the scale on which it was observed by ESEM? Yes, but only in the sense of a statistical average. Many points must be measured and averaged in order to obtain a meaningful result, as has been done in this paper.

An examination of the physical situation being studied also confirms the applicability of this technique. Take, for example, the C–S–H layers in a single C–S–H particle such as that shown in Fig. 2a. The outer circle (labelled *Before shrinkage*) indicates the outer limits of the C–S–H in a wet state; the inner circle (labelled *After shrinkage*) indicates the new C–S–H limit as drying shrinkage occurs. On the assumption that this shrinkage is homogeneous and isotropic, a pair of similar triangles may be drawn from the centre of the C_3S particle to any point on its outer edge, as shown in Fig. 2b. For similar triangles, it is known that

$$\frac{l_1}{l_2} = \frac{x_1}{x_2} \tag{10}$$

indicating that the projection of the outer radius (the x values) will scale directly with the change in length of the outer radius (the l values). More explicitly, the strain along the l direction is given by

$$\varepsilon_l = \frac{l_2 - l_1}{l_1} \tag{11}$$

Similarly, the strain along the x direction is given by

$$\varepsilon_x = \frac{x_2 - x_1}{x_1} \tag{12}$$

Rearranging Equation 10 and substituting into Equation 12 give

$$\begin{aligned} \varepsilon_x &= \frac{x_2 - (l_1/l_2)x_2}{(l_1/l_2)x_2} = \frac{1 - (l_1/l_2)}{l_1/l_2} \\ &= \frac{l_2 - l_1}{l_1} = \varepsilon_l \end{aligned} \tag{13}$$

Thus, the strain along the x direction is identical to that in the l direction.

Two problems may be anticipated in this approach. First, there is an obvious singularity directly perpendicular to the fracture plane. For example, if z_1 or z_2 is taken so that it is drawn straight up from the centre of the particle, as shown in Fig. 2c, shrinkage will occur

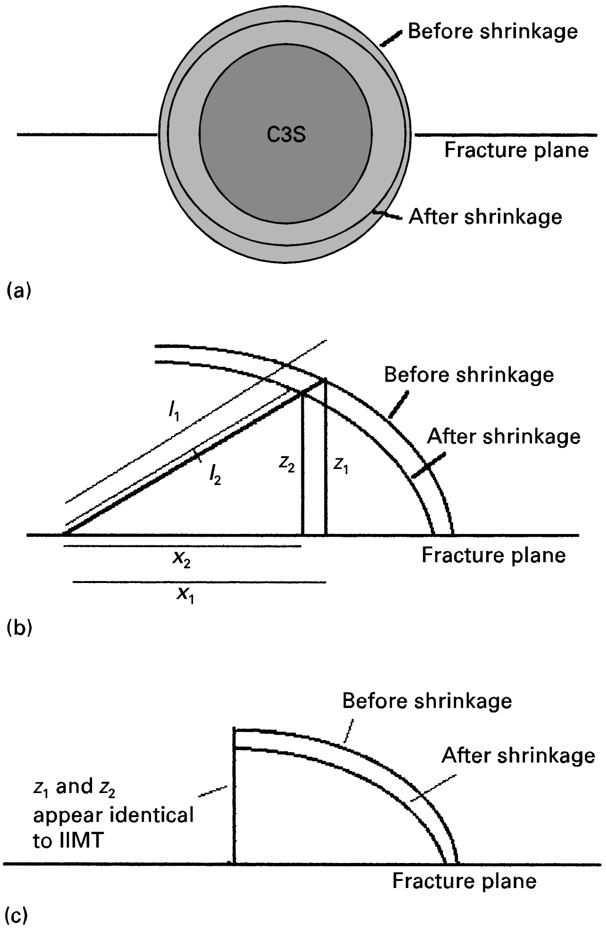

Figure 2 Consideration of 2D versus 3D effects: (a) example of particle on surface showing outer radius of surrounding C–S–H before and after shrinkage (dark grey, C_3S; light grey, C–S–H); (b) similar triangles created by shrinkage shown in (a); (c) representation of singularity for points lying directly above the centre of the particle.

in the z direction and will not be evident to the IIMT, which measures only x and y displacements. This is unavoidable, but for each particle it should only occur once. Thus, this situation applies to very few points in a large field and so does not significantly affect the analysis. Second, what if the layers rearrange or move without shrinking? This is possible, but highly unlikely, except on a very small scale owing to the densely layered nature of C–S–H [1, 2]. The interlayer distances in C–S–H are on the nanometre scale, providing very little room for movement of a single layer. It is comparable with moving one page in a closed book. Thus, any 2D versus 3D conflicts which will occur because of use of the IIMT algorithm will be minimal and have no significant effect on the validity of the data reported in this paper.

3. Experimental results

The values presented are from samples which, to our knowledge, are the smallest specimens to date on which shrinkage has been measured directly. This paper, therefore, reports results that we believe provide better values than can be attained by other techniques, but they are still approximations to a truly unrestrained specimen.

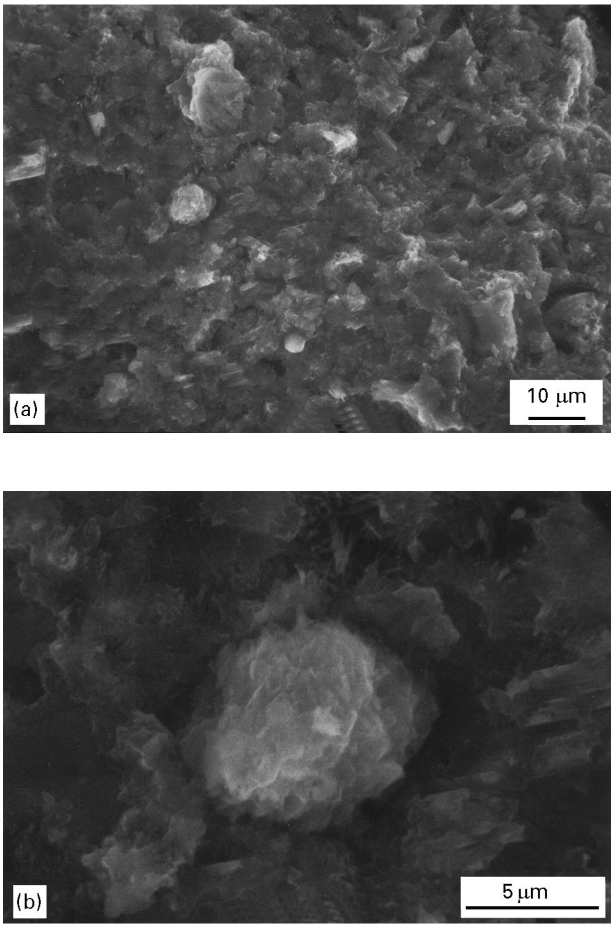

Figure 3 Typical cement paste images for determination of (a) area and (b) particle shrinkages.

Fig. 3 shows typical area and particle regions as defined in Section 2.2 previously. Fig. 3a shows an area approximately 100 μm across, including pores, and Fig. 3b shows a single particle that appears to be relatively detached from the rest of the matrix. Here, the region analysed is only this particle. Results of strain analysis for a variety of samples are shown in Figs 4–6.

3.1. Effects of age

Fig. 4a and b show area and particle shrinkage values, respectively, for 7, 14 and 28 day old cement samples with $w/c = 0.5$ cured at 20 °C. The area shrinkage and the particle shrinkage decrease with increasing age of the specimen. Area shrinkage is significantly smaller than the particle shrinkage at all ages, because of the presence of the restraining phases in the cement paste that reduce how much the C–S–H can shrink.

At intermediate humidities (40–80%), both area shrinkage and particle shrinkage at early ages are relatively large but, at later ages, these values are significantly lower. This suggests that the stresses associated with capillary tension, which is the predominant mechanism at intermediate relative humidities [6], have a decreasing effect on shrinkage at later ages.

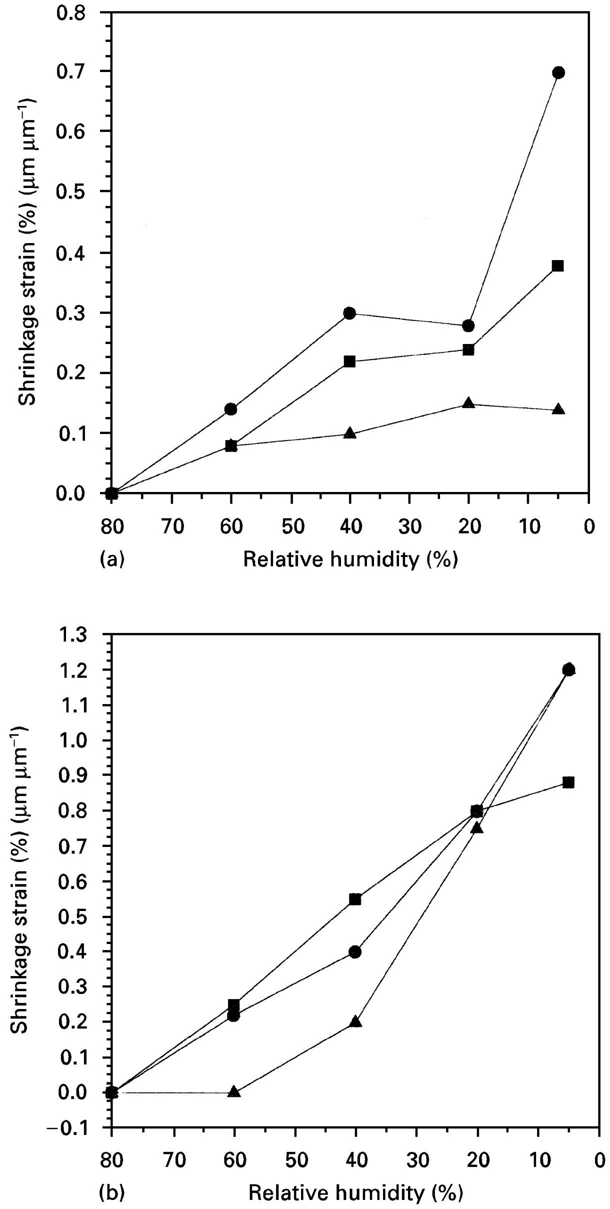

Figure 4 (a) Area, and (b) particle shrinkages at various ages for a cement paste of $w/c = 0.5$ cured at 20 °C. (●), 7 days; (■), 14 days; (▲), 28 days.

This is probably a combination of two different mechanisms:

1. The pore space decreases as the pores fill with hydration product. Less pore space means that fewer menisci can form, with less water having a high capillary tension, which should result in lower overall shrinkage strains.

2. As time passes, C–S–H ages and becomes stronger and, therefore, shrinks less in an *unrestrained* (particle) condition, as discussed by Bazant [19]. The overall modulus of the paste also increases with age, owing to hydration, and so the stiffer paste will shrink less under the same stresses.

At low humidities, particle shrinkage is similar for different ages while area shrinkage shows large differences. The particle shrinkage values are probably due to water loss in the interlayer spaces and changes in surface energy which pull C–S–H particles together. Because the values are similar, it suggests that these mechanisms for shrinkage at low relative humidities are unchanged with age. Thus, the large differences in area shrinkage are due to the arrangement and volume fractions of shrinking and non-shrinking phases, and the amount of capillary porosity, which changes with age. Again, the overall stiffness of cement paste increases with time, which would tend to decrease the area shrinkage.

3.2. Effects of *w/c*

Fig. 5a and b compare the area and particle shrinkages, respectively, for 28-day-old samples of cement pastes cured at 20 °C, with four different *w/c* ratios. In general, higher *w/c* ratios produce higher area and particle shrinkages. This is not surprising, as higher *w/c* values provide more porosity, resulting in a more open microstructure. Area shrinkage values are increased at intermediate humidities owing to the increased capillary porosity that reduces the stiffness of the cement paste, allowing capillary tension to be more effective in causing shrinkage.

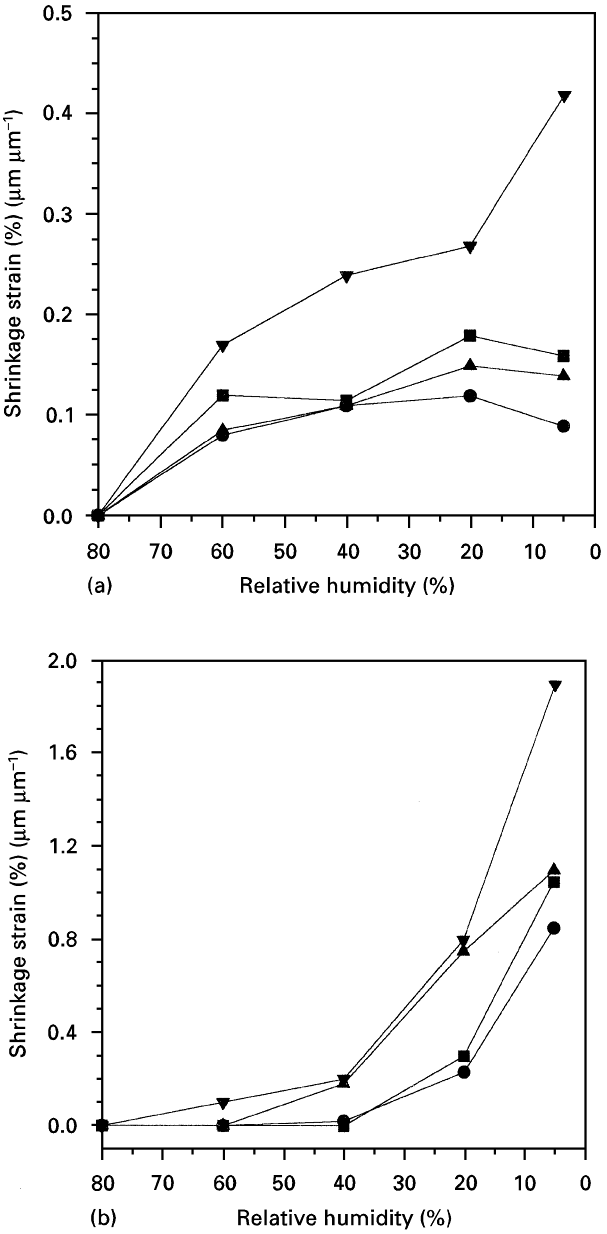

Figure 5 (a) Area, and (b) particle shrinkages at various *w/c* for 28-day-old cement paste cured at 20 °C. (●), $w/c = 0.3$; (■), $w/c = 0.4$; (▲), $w/c = 0.5$; (▼), $w/c = 0.6$.

Particle shrinkage values are similarly higher for higher *w/c* ratios, again owing to the increased porosity. It is interesting to note that, for $w/c = 0.6$, the particle shrinkage at 5% relative humidity is significantly higher than for the other *w/c* values, suggesting a fundamental change in the mechanisms operating in the low humidity range. It is possible that the increased porosity makes removal of the adsorbed and interlayer water much easier, accounting for this result. Models of cement paste predict that, for $w/c \geqslant 0.6$, the capillary porosity is always percolated and therefore open for water transport [20]. However, because of the necessity of increasing the relative humidity to 20% before taking these images, it is impossible to draw definitive conclusions from the 5% relative humidity data.

3.3. Effects of curing temperature

As shown in Fig. 6a and b for samples with $w/c = 0.5$ at 28 days of age, shrinkage of both areas and particles is reduced by curing at higher temperatures. However, there was only a small influence of temperature on the degree of reaction obtained at 28 days, as LOI obtained results of 83.2%, 84.8% and 85.4% reacted when cured at 20 °C, 30 °C and 40 °C, respectively. Even though higher temperatures do accelerate cement hydration, 28 days was a sufficiently long period of time for even the cement paste at the lowest curing temperature to achieve nearly full hydration. That higher curing temperatures, at equal degrees of hydration, should produce lower shrinkage is surprising, as it has been found that a greater volume and coarser distribution of capillary porosity is produced at higher curing temperatures [21]. However, this same work also found that surface area (measured by water) was decreased by higher curing temperatures. Thus, since many of the shrinkage mechanisms are surface area related, this could account for these results. The shrinkage at low relative humidities, paste the capillary condensation point, is proportional to the surface area of the regions which have an adsorbed water film [22]. Higher temperatures should also increase silicon diffusion rates, allowing for increased silicate polymerization [23–25]. This would imply higher C–S–H moduli and different C–S–H layer structures, which may also account for a change in shrinkage mechanisms and a reduction in shrinkage.

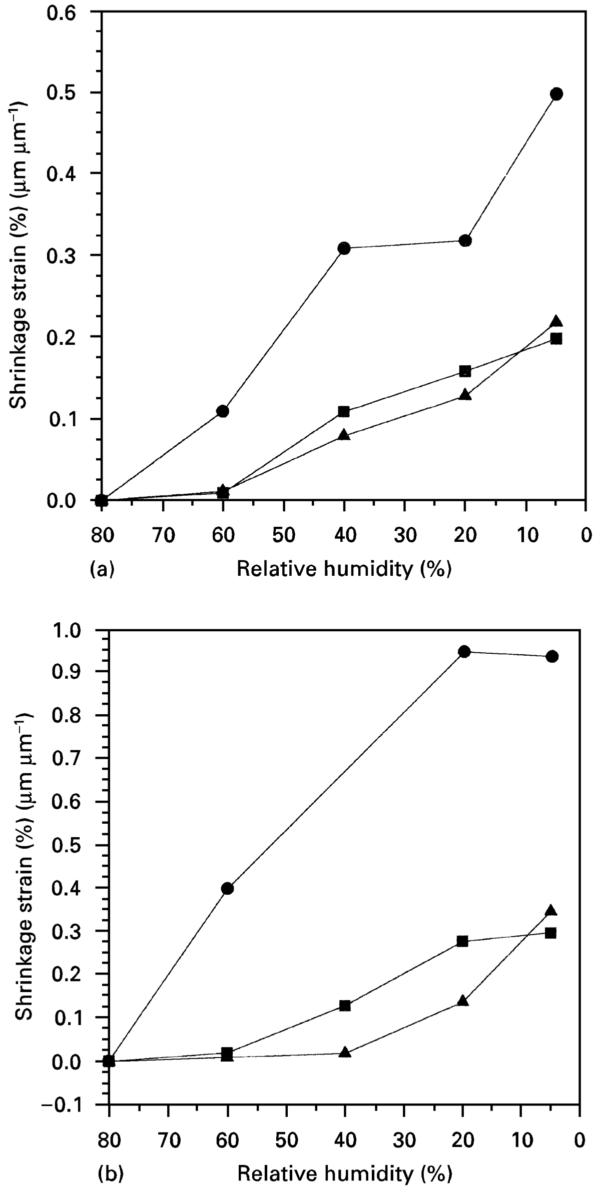

Figure 6 (a) Area, and (b) particle shrinkages at various curing temperatures for 28-day-old cement paste of $w/c = 0.5$. (●), 20 °C; (■), 30 °C; (▲), 40 °C.

4. Comparison with models of shrinkage

4.1. Hydration model

In order to interpret our experimental results of the shrinkage of C–S–H in small areas or single particles, two modifications have been made to the basic 3D hydration model developed by Bentz and Garboczi [26]. Their model uses the algorithm that a hydrating C_3S grain produces 1.71 pixels of C–S–H and 0.61 pixels of CH, where a pixel usually has an edge length of 1 μm. One C–S–H pixel is placed in close proximity to the C_3S pixel from which it was generated, while the additional 0.71 pixel of C–S–H and 0.61 pixel of CH are placed randomly within the available pore volume. The first modification allowed the additional C–S–H to form only within a cube with sides of 11 pixels, centred on the dissolving C_3S pixel. This resulted in C–S–H that formed close to its hydrating C_3S source particle in the model. CH was still placed randomly within the entire pore volume.

A second modification used for the simulations separated the C–S–H into two types with different densities. Jennings and Tennis [27, 28] have noted that C–S–H can be divided into two subsets, one having a much higher density than the other. The high-density C–S–H is sometimes described as phenograins [29] or inner product, the C–S–H gel which forms within or near the boundary of the original C–S–H particle. However, because phenograins may include CH, clinker and other dense parts of the microstructure, and because the inner product is not always dense, the label HD C–S–H is used here. For similar reasons, the low-density C–S–H, sometimes described as ground mass [29] or outer product, which is a more open and less dense structure that forms in the pore

TABLE I Volume ratio, V_{ratio}, LD C–S–H to total C–S–H ratio of the volume, $V_{\text{LD C–S–H}}$, LD C–S–H, and appropriate conversion data for the basic hydration model

w/c	V_{ratio} (%)	γ	*x* (%)	Type of conversion
Basic model	41.5	0.71		
0.3	34.3	0.52	12.38	LD C–S–H → HD C–S–H
0.4	41.3	0.70	0	None
0.5	48.4	0.94	11.76	HD C–S–H → LD C–S–H
0.6	55.5	1.25	23.84	HD C–S–H → LD C–S–H

space outside the original C_3S grain, will be referred to as LD C–S–H. In order to estimate the amounts of LD C–S–H and HD C–S–H, the model of Jennings and Tennis [27, 28] was used. In that model, it was assumed that the nitrogen-accessible C–S–H was the low-density product and that the nitrogen-inaccessible C–S–H was the high-density product. The ratio, V_{ratio}, of the volume, $V_{\text{LD C–S–H}}$, of nitrogen-accessible C–S–H to the volume, $V_{\text{C–S–H}}$, of total C–S–H increases with increasing *w/c* ratio according to

$$V_{\text{ratio}} = \frac{V_{\text{LD C–S–H}}}{V_{\text{C–S–H}}} = 0.706\frac{w}{c} + 0.131 \quad (14)$$

Values for V_{ratio} as predicted by Equation 14 were determined for a range of *w/c* values and are shown in Table I. Also shown in Table I are the ratio of LD C–S–H to HD C–S–H which have been calculated through

$$V_{\text{C–S–H}} = V_{\text{LD C–S–H}} + V_{\text{HD C–S–H}} \quad (15)$$

Rearranging Equation 15 and dividing Equation 14 by the rearranged Equation 15 determines the ratio of LD C–S–H to HD C–S–H, hereafter referred to as γ:

$$\gamma = \frac{V_{\text{LD C–S–H}}}{V_{\text{HD C–S–H}}} = \frac{0.706w/c + 0.131}{0.869 - 0.706w/c} \quad (16)$$

These data can be compared with similar ratios for the basic hydration model described above where the C–S–H pixel generated in close proximity to the C_3S grain from which it was generated is defined as high-density product, and the additional 0.71 pixels of C–S–H defined as low-density product. Thus, the basic hydration model has a constant value of 0.71 for γ.

In order to account for changes in V_{ratio} and γ for various *w/c* ratios in the hydration model, it becomes necessary to convert C–S–H from one type to another. Observation of Table I shows that for $w/c = 0.3$, it is necessary to convert some LD C–S–H into HD C–S–H and that, for $w/c = 0.5$ or $w/c = 0.6$, conversion from HD C–S–H to LD C–S–H is necessary. At $w/c = 0.4$, the basic hydration model is satisfactory in its distribution. Taking x as the fraction of C–S–H that must be converted, for $w/c = 0.3$,

$$\gamma = \frac{0.71 - x}{1 + x} \rightarrow x = \frac{0.71 - \gamma}{1 + \gamma} \quad (17)$$

is applicable and for $w/c = 0.5$ or 0.6,

$$\gamma = \frac{0.71 + x}{1 - x} \rightarrow x = \frac{\gamma - 0.71}{1 + \gamma} \quad (18)$$

is applicable. Calculated values for x and the appropriate kind of conversion are also shown in Table I for the different *w/c* ratios. These conversions were introduced into the pixel model by assigning an appropriate chance for conversion, x, from one type of C–S–H to the other type to each C–S–H pixel generated. This modified pixel model was then used to simulate microstructures for various *w/c* ratios and degrees of hydration. A 256^3 pixel system was used together with the particle size distribution for C_3S grains listed in Table II [30]. The possible effect of different cement particle size distributions and degrees of flocculation were not considered in this study.

TABLE II C_3S particle size distribution for hydration simulation [30]

Diameter (μm)	Distribution (vol %)
19	21
17	4
15	9
13	9
11	9
9	11
7	9
5	10
3	10
1	8

4.2. Shrinkage model

Following hydration, ten slices were cut from each of the model microstructures and drying shrinkage was modelled using a finite-element model, which has been described in detail elsewhere [13, 31]. Each pixel is treated as a simple bilinear finite element, with the finite-element nodes of the problem located at the pixel corners. The moduli of each pixel are defined by its phase label. Each phase is assigned values of Young's modulus, Poisson's ratio and unrestrained shrinkage strain parameter, ε_i. In order to compute the shrinkage, the size of the system, in addition to the nodal displacements, is treated as a dynamic variable and so is allowed to vary in order to mininize the elastic energy. Each phase has a certain unrestrained shrinkage (particle shrinkage) which competes with the rigidity of the rest of the system to produce an overall shrinkage (area shrinkage). When the elastic strain energy is minimized, the average stress is zero, but the individual stresses in each pixel are generally non-zero. The overall composite shrinkage, ε^*, and the nodal displacements are reported by the program. Only reversible linear elastic shrinkage is considered.

4.2.1. Three-dimensional versus two-dimensional considerations

Using a 2D model to study the measured 3D strains does introduce some error due to several assumptions made in the modelling process. The first assumption is that the 3D cement paste microstructural model does a good job of reproducing the 3D microstructure. Then, by taking 2D slices of this model, converting the moduli of each phase to its 2D plane-stress equivalent, and then putting in an intrinsic shrinkage for the C–S–H, the overall effective sample shrinkage is computed. The second assumption is then that this is equivalent to running the full elastic analysis on the 3D model. This is not correct in general but, as we shall see, is a reasonably good approximation.

Two exact examples will suffice to illustrate this point. The first is the equal shear modulus case. For any two-phase microstructure, with volume fractions, c_1 and c_2, if each phase is elastically isotropic and the shear moduli in both phases are equal, then the effective bulk and shear modulus of the system can be found exactly. A slice will give another randomly chosen microstructure, with area fractions equal to the volume fractions of the original, whose moduli can again be found exactly. The effective shear modulus is just the equal shear moduli of the phases, while the bulk modulus is given by [32, 33]

$$K = \frac{\frac{4}{3}G(c_1K_1 + c_2K_2) + K_1K_2}{\frac{4}{3}G + c_1K_2 + c_1K_1} \quad \text{for three dimensions} \tag{19}$$

and

$$K = \frac{G(c_1K_1 + c_2K_2) + K_1K_2}{G + c_1K_2 + c_2K_1} \quad \text{for two dimensions} \tag{20}$$

The second example is that of a dilute suspension of spherically shaped inclusions in a matrix, with all materials elastically isotropic. The spheres can have any size distribution. Taking a slice of this system will produce a suspension of circular shaped inclusions, with a different size distribution, but with area fractions equal to the volume fractions of the original system. If phase 1 is the matrix, and phase 2 is the inclusions, then the bulk modulus of the system is [33, 34]

$$\frac{1}{K} = \frac{1}{K_1} + \frac{c_2(1/K_2 - 1/K_1)(1/K_1 + \frac{3}{4}G)}{1/K_2 + \frac{3}{4}G} \quad \text{for three dimensions} \tag{21}$$

and

$$\frac{1}{K} = \frac{1}{K_1} + \frac{c_2(1/K_2 - 1/K_1)(1/K_1 + 1/G)}{1/K_2 + 1/G} \quad \text{for two dimensions} \tag{22}$$

For two-phase systems, with an intrinsic shrinkage (or thermal strain) of α_i in each phase, the effective composite shrinkage is given exactly, in two or three dimensions, by the Rosen–Hashin [35] equation

$$\alpha = c_1\alpha + c_2\alpha_2 + \frac{\alpha_2 - \alpha_1}{1/K_2 - 1/K_1}\left(\frac{1}{K} - \frac{c_1}{K_1} - \frac{c_2}{K_2}\right) \tag{23}$$

where c_i is a volume fraction or an area fraction.

Therefore, to illustrate the comparison between two and three dimensions, we first choose values of K_1, K_2, G_1, G_2, α_1 and α_2 in three dimensions. These are inserted into the equations for the 3D effective bulk modulus, and then into the Rosen–Hashin equation to get the effective overall shrinkage. These phase moduli are then converted to their plane stress equivalents, inserted into the expressions for the 2D effective bulk modulus, and then inserted into the Rosen–Hashin equation to get the effective 2D shrinkage. The exact effective shrinkage values in two and three-dimensions are then compared.

For the equal shear modulus case, take $K_1 = 1$, $G_1 = G_2 = 1$ and $\alpha_2 = 0$, with $c_1 = c_2 = 0.5$. The value of α_1 is arbitrary, and K_2 is taken over a range from 1 to 100. Results are presented in terms of α/α_1; so, when $K_2 = K_1 = 1$, the value of α/α_1 is exactly c_1 or 0.5 since, when the two phases have the same moduli, the shrinkage is exactly given by $\alpha = c_1\alpha_1 + c_2\alpha_2$, which is Vegard's law.

For the dilute spherical inclusion microstructure, $K_1 = 1$, $G_1 = 1$ and $K_2/K_1 = G_2/G_1$ so that the phases have the same Poisson's ratio [36], and $\alpha_2 = 0$, with c_2 arbitrary. In this case, the spherical inclusions can be thought of as a restraining phase. The effective shrinkage can be written as

$$\alpha = \alpha_1(1 - fc_2) \tag{24}$$

with the coefficients f_{2D} and f_{3D} determining the shrinkage response. In the limit of equal moduli in each phase, both f_{2D} and f_{3D} reduce to 1.

Fig. 7a and b shows the parameters for the two exact examples. The 2D and 3D parameters are equal in the uniform material case, which is not surprising, but become increasingly different as the bulk moduli become farther apart. However, the difference is not that great, lending support to the possibility of using a 2D model to interpret the 3D measurements. In Fig. 7a and b, the region of interest is probably where K_2/K_1 is of the order of 50 or more, since the moduli of cement are around 50 or so times those for C–S–H (see next section).

A numerical example which elucidates this difference between two and three dimensions more exactly for the cement paste system of interest uses the full 3D model microstructure. The 3D version of the shrinkage code has only recently been developed [31]. A cement paste microstructure was created, elastic moduli as described in the next section were assigned to the phases, and an intrinsic shrinkage of 0.01 was assigned to the entire C–S–H phase. The same thing was done for five slices, but with phase moduli replaced by their plane-stress equivalents. *w/c* ratios of 0.3, 0.4, 0.5 and

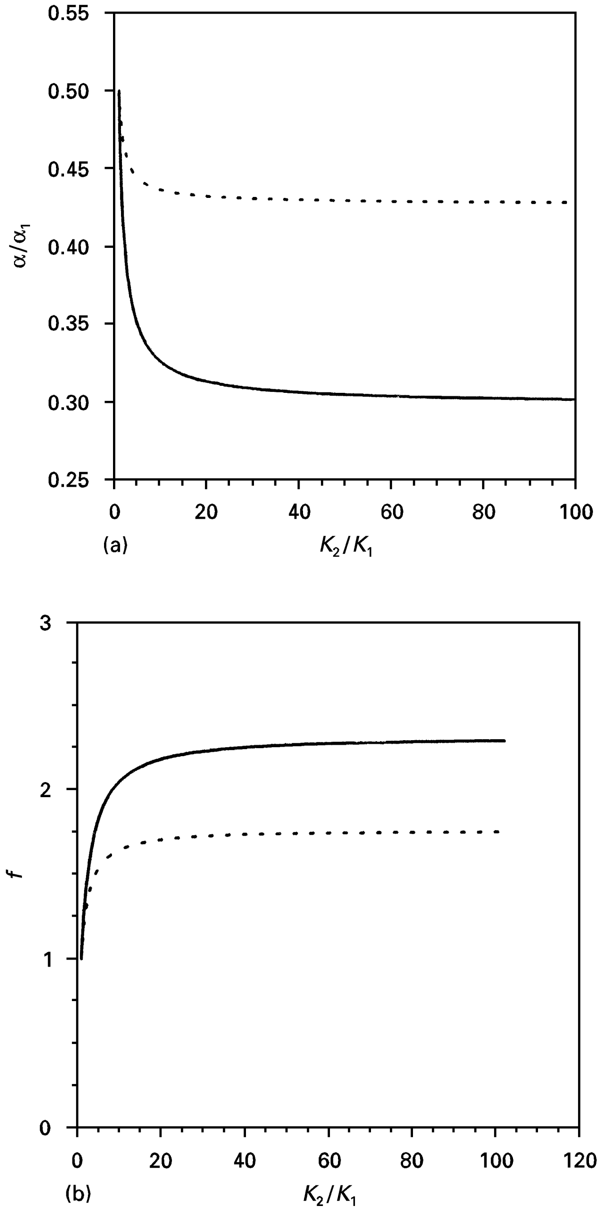

Figure 7 Comparison of parameters for exact examples. (a) Effective shrinkages, α/α_1 for equal shear moduli example. (——), three dimensions; (– – –), two dimensions. (b) Shrinkage coefficients f_{2D} (– – –) and f_{3D} (——) for dilute limit of spherical inclusions.

0.6 were used, at about 65% hydration. Table III shows the results. For w/c values between 0.3 and 0.5, the average effective shrinkage as computed on the slices tends to be about 20% higher in magnitude than the 3D shrinkages. The reverse was found for $w/c = 0.6$.

It is obvious that the 2D representation is not perfect in its description of the 3D shrinkage being experimentally measured. However, the authors believe that these models can provide valuable insights into the shrinkage behaviour of cement pastes and are justified in their presentation. Further analyses using the 3D code are necessary to increase the accuracy of these results but at present are limited by the long run times necessary to analyse many systems, even with a small system approximately 100^3 pixels in size. Larger systems than this in three dimensions take impractically long run times to analyse, so that the resolution available for 3D analysis is limited. As the computing power barrier is removed, this issue will be explored in more depth.

TABLE III Comparison of normalized effective shrinkages predicted by 2D and 3D models for various w/c cement paste models

w/c	Effective shrinkage/intrinsic shrinkage of C–S–H	
	3D	2D
0.3	0.28	0.38
0.4	0.32	0.4
0.5	0.34	0.37
0.6	0.37	0.28

4.2.2. Approximation of C–S–H elastic moduli

The values of Young's modulus, Poisson's ratio and unrestrained shrinkage for each phase in the model microstructure are shown in Table IV. Vernet [37] has determined values of $E_{C3S} = 117.70$ GPa and $\nu_{C3S} = 0.31$ for C_3S or, equivalently, $K_{C3S} = 103.25$ GPa and $G_{C3S} = 44.92$ GPa via [17]

$$K = \frac{E}{3(1-2\nu)} \tag{25}$$

$$G = \frac{E}{2(1+\nu)} \tag{26}$$

Values from Monteiro and Chang [38] were used for the Young's modulus and Poisson's ratio of CH; their work gave values of $E_{CH} = 43$ GPa and $\nu_{CH} = 0.32$, which results in $K_{CH} = 39.8$ GPa and $G_{CH} = 16.3$ GPa. Pores were given values of zero for Young's modulus and Poisson's ratio. All three of these phases were assumed to be non-shrinking. While this may seem inaccurate in the case of pores where capillary stress occurs, the actual displacement occurs in the C–S–H layers; therefore, any shrinkage arising from capillary stress is assigned to the intrinsic shrinkage strain of C–S–H.

Since no data exist on the elastic properties of the C–S–H phase, it was necessary to approximate these values from available data. Helmuth and Turk [39] measured the values of Young's modulus and Poisson's ratio for cement and C_3S pastes as a function of capillary porosity. For C_3S pastes, extrapolation to zero capillary porosity produced values of $E_{gel} = 4.69$ GPa and $\nu_{gel} = 0.25$ for the gel, where in the notation of Helmuth and Turk this was a solid mixture consisting of CH and C–S–H. This gives $K_{gel} = 3.13$ GPa and $G_{gel} = 1.88$ GPa.

TABLE IV Elastic moduli used in shrinkage simulations

Phase	E (GPa)	ν	ε_i	Reference
C_3S	117.70	0.31	0	[37]
CH	43.00	0.32	0	[38]
C–S–H	2.60	0.26	Varies	
Pore	0	0	0	

It is now necessary to divide the gel into CH and C–S–H. As mentioned previously, the hydration model produces 1.71 pixels of C–S–H for each 0.61 pixels of CH produced. This results in relative volume fractions of $v_{\mathrm{CH}} = 26.3\%$ and $v_{\text{C–S–H}} = 73.7\%$, where v_{CH} and $v_{\text{C–S–H}}$ are the volume fractions of CH and C–S–H, respectively.

To calculate elastic values for C–S–H, the gel was treated as a composite consisting of CH and C–S–H. A 3D effective medium theory for spherical inclusions developed by Berryman [40] was used. It is obviously unrealistic to consider CH crystals as spherical, but it offers a first approximation for the elastic moduli of the C–S–H. The following equations were solved numerically to calculate values for the bulk and shear modulus of C–S–H:

$$\frac{1}{K^* + \frac{4}{3}G^*} = \sum_{i=1}^{n} \frac{v_i}{K_i + \frac{4}{3}G^*} \tag{27}$$

$$\frac{1}{G^* + F^*} = \sum_{i=1}^{n} \frac{v_i}{G_i + F^*} \tag{28}$$

$$F^* = \frac{G^*}{6}\frac{9K^* + 8G^*}{K^* + 2G^*} \tag{29}$$

where K^* and G^* are the bulk and shear moduli, respectively, of the composite, in this case the hydration gel, v_i, K_i and G_i are the volume fraction, bulk and shear moduli, respectively, of each phase, and $n = 2$. Using this technique, values of $K_{\text{C–S–H solid}} = 1.80$ GPa and $G_{\text{C–S–H solid}} = 1.03$ GPa were calculated, giving $E_{\text{C–S–H solid}} = 2.60$ GPa and $\nu_{\text{C–S–H solid}} = 0.26$ via Equations 25 and 26.

4.2.3. Shrinkage simulations

A range of values for intrinsic (particle) shrinkage was used to predict values of effective (area) shrinkage. Two sets of simulations were run. In both sets, the same values of elastic moduli were used for both LD C–S–H and HD C–S–H as determined above. In the first set, all the C–S–H was assumed to be a shrinking phase. Unrestrained shrinkages of -5% and -1% were used for C–S–H to determine composite shrinkage. In the second set of simulations, LD C–S–H and HD C–S–H were treated separately. Only the LD C–S–H was allowed to shrink, again using values of -5% and -1% for the unrestrained shrinkage of LD C–S–H. The differences in the distribution of shrinking phase caused by these two contrasting simulations are shown in Fig. 8a and b. Fig. 8a shows all the C–S–H phase in white, while Fig. 8b shows only the LD C–S–H product, as determined by the microstructure model, in white.

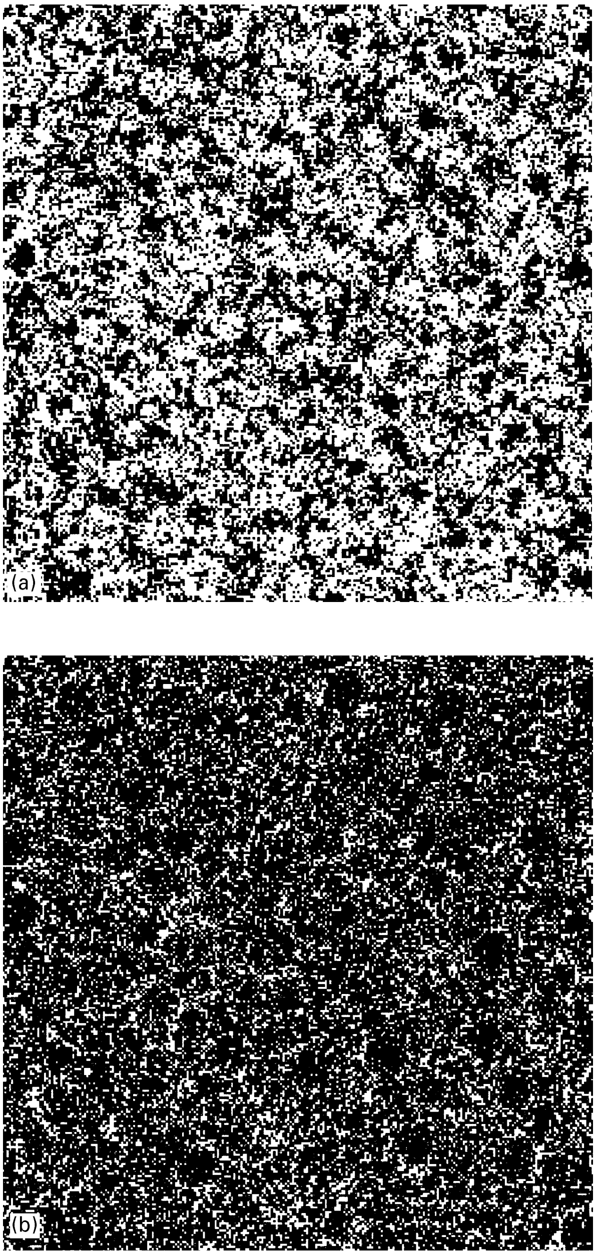

Figure 8 Distribution of shrinking phase for (a) all C–S–H shrinking and (b) only LD C–S–H shrinking. White, shrinking phase; black, non-shrinking phase.

It may seem odd to consider a situation in which only the LD C–S–H shrinks. Consider, however, the physical distribution of the phases. To a first approximation, a hydrated C_3S (or cement) particle may be considered as a series of three spheres centered on the same point. In the interior is the unhydrated material, surrounded by a shell of HD C–S–H, which is in turn surrounded by a shell of LD C–S–H. Only the LD C–S–H is in contact with the capillary porosity, the pathways by which most moisture removal will occur. It would follow that during drying the LD C–S–H will lose its moisture earlier and to a much greater degree than the HD C–S–H. If the removal of this moisture causes C–S–H layer collapse, as has been proposed by Feldman and Sereda [2], this may limit moisture removal from the HD C–S–H, causing little to no shrinkage in this phase. It would then be natural to model the C–S–H as having shrinkage properties only in the less dense region. This argument from the topology of the C–S–H surrounding a cement grain implies that there could be shrinkage differences between the low-density and high-density products even if there were no compositional differences.

As noted above, one output from the model is a composite shrinkage value, ε*. This composite shrinkage value can be compared directly with the area shrinkage measured by ESEM. Because C–S–H is considered to be the only shrinking phase, it is then possible, in the model, to vary the value of the intrinsic shrinkage, $\varepsilon_{C\text{–}S\text{–}H}$, of C–S–H so as to match the model's composite shrinkage value to the experimentally measured area shrinkage. This value for the intrinsic shrinkage of C–S–H, determined in the model, can then be compared with the experimentally measured *particle* shrinkage values, which approach the true intrinsic shrinkage values of the C–S–H. In this way, the experimentally measured area shrinkage values are used to calibrate the model parameters for intrinsic shrinkage.

Comparison of the modelling results for intrinsic shrinkage with the experimentally measured particle shrinkage show reasonable agreement over the entire relative humidity scale when only the LC C–S–H is allowed to shrink. However, if composite shrinkage is modelled with all the C–S–H shrinking, then the value determined in the model for *intrinsic* shrinkage does not agree with the experimentally measured value for particle shrinkage. Fig. 9 shows typical results for a system with $w/c = 0.3$ and degree of hydration of 66%. It is clear that the model values for intrinsic shrinkage, when only LD C–S–H shrinks, follow the same trend and are much closer in magnitude to the experimentally measured values than those model values determined in the case when all the C–S–H phase is allowed to shrink. A noticeable deviation from the model trends occurs after equilibration at 5% relative humidity. As noted previously, the necessity of raising the relative humidity to 20% before imaging at this point makes results at 5% relative humidity the most uncertain of all the data.

It is interesting to note that the model values with only the LD C–S–H shrinking are slightly larger than the experimentally measured values for the intrinsic shrinkage of C–S–H. It is possible that, even in the small-scale particle studies presented in this paper, the restraining effect of the matrix limits the particle shrinkage somewhat. This effect would cause the measured particle shrinkages to be less than the true intrinsic shrinkage of C–S–H. Since there is always some restraint present, it is true in general that the particle shrinkage will always be somewhat less than the true intrinsic shrinkage. This suggests that it is very difficult to measure experimentally intrinsic shrinkage of C–S–H and that only through the combination of experiment and modelling will the true intrinsic shrinkage of C–S–H be resolved.

The above effect is probably more pronounced than is shown in Fig. 9, because of the 2D versus 3D comparison previously considered. For $w/c = 0.30$, the 2D version of the model gave a higher composite shrinkage than did the 3D version, for the same intrinsic shrinkage. This suggests that, if the 3D code was used for all this work, a *higher* value of C–S–H intrinsic shrinkage would have been needed in the model in order to be able to match the experimental area shrinkage measurement, probably of the order of about 25% higher. This would increase the discrepancy between the measured particle shrinkage and the fitted intrinsic model shrinkage. There were also certainly viscoelastic effects in the experiment, which would give more apparent shrinkage strain for the same elastic intrinsic shrinkage. Matching these values with a purely linear elastic model would also then tend to give too high model intrinsic shrinkages.

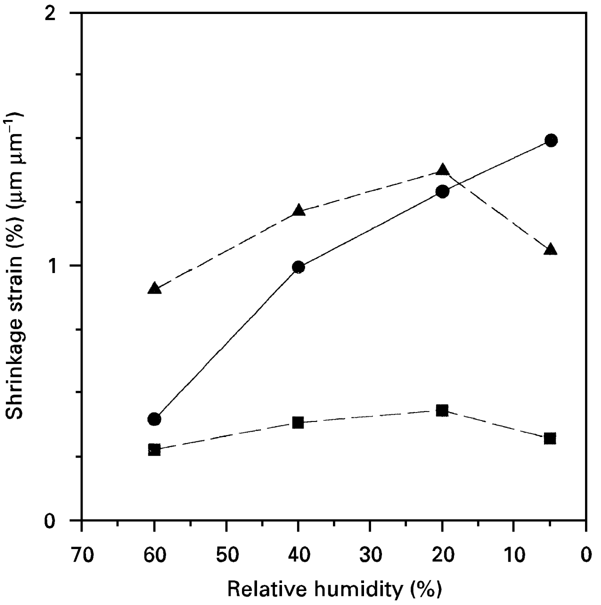

Figure 9 Comparison of intrinsic (particle) shrinkage results between experimentally measured values (●) and model results ((■), all C–S–H shrinking; (▲), outer C–S–H shrinking) for a system of $w/c = 0.3$ and degree of hydration of 66%.

Given these considerations, the observation that intrinsic shrinkages found in the model when all the C–S–H was made a shrinking phase were *less* the experimental measurements strengthens the argument that not all the C–S–H actively participates in the shrinkage. If all the C–S–H actively participates in the shrinkage, one would then expect to find the model data were greater than the experimental data and not less. Making all the C–S–H a shrinking phase gives too much shrinkage for a given assigned intrinsic shrinkage, again implying that not all the C–S–H actively shrinks. While the agreement is certainly not perfect and, given the number of assumptions which have been made, one would not expect it to be, the trend of the data in Fig. 9 does suggest that it is only the volume of C–S–H measured by nitrogen surface area, which is defined to be LD C–S–H in this paper, that controls the shrinkage of cement-based materials, especially at lower relative humidities. This may be a result of compositional differences, or a reflection of the topology of the LD C–S–H and HD C–S–H surrounding a cement grain, or a combination of both effects.

5. Summary

This paper has reported initial results of shrinkage at the micrometre level in cement paste and mortars. A new image analysis technique was used to measure strain *in situ* within an environmental scanning electron microscope. Although these results can only be considered preliminary, they provide insight into microstructural changes that occur upon drying of cement-based materials.

Observations have confirmed that strains at the scale of several hundreds of micrometres have similar trends to the strains measured on larger specimens. The specimens are small enough to preclude differential shrinkage due to moisture gradients. Shrinkage at this scale can be considered *real* shrinkage as defined by Wittmann [12]. Shrinkage is greatest for young specimens with high *w/c* ratios. High temperature curing decreases shrinkage, even at equivalent degrees of hydration. These result suggest that C–S–H ages as the reaction proceeds and grows stronger, making it more resistant to shrinkage. Intermediate relative humidity shrinkage mechanisms, such as capillary stress, are independent of *w/c* ratio and age, although the shrinkage that they induce of course depends on the elastic moduli, pore size and porosity of the cement paste, which are functions of these variables.

Values of shrinkage across a distance of hundreds of micrometres are significantly smaller than shrinkage of an individual, nearly unrestrained particle of C–S–H. The value for unrestrained shrinkage may be used for modelling the *real* shrinkage. Results from model and experiment agree reasonably well when values for unrestrained shrinkage (i.e., particle shrinkage) measured in experiment are used in the model and when the volume of the shrinking phase is only a subset of the total C–S–H in the system. The volume of this sub-phase is determined by the Jennings–Tennis [27, 28] model that rationalizes nitrogen surface area observations, dividing C–S–H into low- and high-density products.

Acknowledgements

We gratefully acknowledge the financial support provided by the US Department of Energy (Award DE-FG02-91ER45460/A01). Part of this research led to a PhD of one of the authors (T.B.B.). C.M.N. wishes to thank the US Department of Defense for funding through a National Defense Science and Engineering Graduate Fellowship.

References

1. R. F. FELDMAN and P. J. SEREDA, *Mater. Constrn.* **1** (1968) 509.
2. *Idem.*, *Engng J.* **53** (1970) 53.
3. X. CONG, PhD Thesis, University of Illinois at Urbana-Champaign (1994).
4. H. F. W. TAYLOR, *J. Amer. Ceram. Soc.* **69** (1986) 464.
5. *Idem.*, "Cement chemistry" (Academic Press, London, 1990).
6. Z. P. BAZANT, in Proceedings of the Fourth RILEM International Symposium on Creep and Shrinkage of Concrete: Mathematical Modeling (Northwestern University, Evanston, IL, 1986) p. 41.
7. S. MINDESS and J. F. YOUNG, "Concrete" (Prentice-Hall, Englewood Cliffs, NJ, 1981).
8. Y. XI and H. M. JENNINGS, in "Materials science of concrete III", edited by J. P. Skalny (American Ceramic Society, Westerville, OH, 1992) p. 37.
9. C. F. FERRARIS and F. H. WITTMANN, *Cem. Concr. Res.* **17** (1987) 453.
10. W. HANSEN, *J. Amer. Ceram. Soc.* **70** (1987) 323.
11. J. A. ALMUDAIHEEM, *J. King Saud Univ., Engng Sci.* **1** (1991) 69.
12. F. H. WITTMANN, in "Fundamental research on creep and shrinkage of concrete", edited by F. H. Wittmann (Martinus Nijhoff, Boston, MA, 1982) p. 129.
13. C. M. NEUBAUER, H. M. JENNINGS and E. J. GARBOCZI, *Adv. Cem. Based Mater.* **4** (1996) 6.
14. H. M. JENNINGS and K. SUJATA, *Mater. Res. Soc. Symp. Proc.* **245** (1992) 243.
15. *Idem.*, *J. Amer. Ceram. Soc.* **75** (1992) 1669.
16. Y. XI, T. B. BERGSTROM and H. M. JENNINGS, *Comput. Mater. Sci.* **2** (1994) 249.
17. T. H. COURTNEY, "Mechanical behavior of materials" (McGraw-Hill, New York, 1990).
18. J. W. EISCHEN and S. TORQUATO, *J. Appl. Phys.* **74** (1993) 159.
19. Z. P. BAZANT, in "Mathematical modeling of creep and shrinkage of concrete", edited by Z. P. Bazant (Wiley, New York, 1988) p. 99.
20. D. P. BENTZ and E. J. GARBOCZI, *Cem. Concr. Res.* **21** (1991) 325.
21. A. BENTUR, R. L. BERGER, J. H. KUNG, N. B. MILESTONE and J. F. YOUNG, *J. Amer. Ceram. Soc.* **62** (1979) 362.
22. G. W. SCHERER, *ibid.* **69** (1986) 473.
23. L. J. PARROTT, *Cem. Concr. Res.* **7** (1977) 597.
24. A. BENTUR, J. H. KUNG, R. L. BERGER, J. F. YOUNG, N. B. MILESTONE, S. MINDESS and F. V. LAWRENCE, in Proceedings of the Seventh International Conference on the Chemistry of Cement **III** (Editions Septima, Paris, 1980) p. V126.
25. M. GEIKER, PhD Thesis, Technical University of Denmark, Copenhagen (1983).
26. D. P. BENTZ and E. J. GARBOCZI, US Department of Commerce, National Institute of Standards and Technology, Gaithersburg, MD, Internal Report 4746 (1992).
27. H. M. JENNINGS and P. D. TENNIS, *J. Amer. Ceram. Soc.* **77** (1994) 3161.
28. *Idem.*, *ibid.* **78** (1995) 2575.
29. S. DIAMOND and D. BONEN, *ibid.* **76** (1993) 2993.
30. R. T. COVERDALE, PhD Thesis, Northwestern University, Evanston, IL (1991).
31. E. J. GARBOCZI, "Finite element and finite difference codes for computing the linear elastic and elastic properties of digital images of random materials", US Department of Commerce, National Institute of Standards and Technology, Gaithersburg, MD, Internal Report, in press (1997).
32. R. HILL, *J. Mech. Phys. Solids* **12** (1964) 199.
33. M. F. THORPE and I. JASIUK, *Proc. R. Soc. A* **438** (1992) 531.
34. R. M. CHRISTENSEN, *Mechanics of composite materials* (John Wiley & Sons, New York, 1979).
35. B. W. ROSEN and Z. HASHIN, *Int. J. Engng Sci.* **8** (1970) 157.
36. E. J. GARBOCZI and A. R. DAY, *J. Mech. Phys. Solids* **43** (1995) 1349.
37. C. VERNET, Private communication to E.J.G.
38. P. J. M. MONTEIRO and C. T. CHANG, *Cem. Concr. Res.* **25** (1995) 1605.
39. R. A. HELMUTH and D. H. TURK, *Highway Res. Board, Spec. Rep.* **90** (1966) 135.
40. J. G. BERRYMAN, *J. Acoust. Soc. Amer.* **68** (1980) 1809.

Received 2 April
and accepted 29 May 1997